JACS
JOURNAL OF THE AMERICAN CHEMICAL SOCIETY
Article
Cite This: J. Am. Chem. Soc. 2018, 140, 12457−12468
pubs.acs.org/JACS

Oxygen-Tolerant H_2 Production by [FeFe]-H_2ase Active Site Mimics Aided by Second Sphere Proton Shuttle

Md Estak Ahmed,[†] Subal Dey,[†] Marcetta Y. Darensbourg,*[,‡] and Abhishek Dey*[,†]

[†]Department of Inorganic Chemistry, Indian Association for the Cultivation of Science, Kolkata 700032, India
[‡]Department of Chemistry, Texas A&M University, College Station, Texas 77843-3255, United States

Supporting Information

ABSTRACT: The instability of [FeFe]-H_2ases and their biomimetics toward O_2 renders them inefficient to implement in practical H_2 generation (HER). Previous investigations on synthetic models as well as natural enzymes proved that reactive oxygen species (ROS) generated on O_2 exposure oxidatively degrades the 2Fe subcluster within the H-cluster active site. Recent electrochemical studies, coupled with theoretical investigations on [FeFe]-H_2ase suggested that selective O_2 reduction to H_2O could eliminate the ROS, and hence, tolerance against oxidative degradation could be achieved (*Nat. Chem.* **2017**, *9*, 88−95). We have prepared a series of 2Fe subsite mimics with substituted arenes attached to bridgehead N atoms in the S to S linker, $(\mu\text{-}S_2(CH_2)_2NAr)[Fe(CO)_3]_2$. Structural analyses find the nature of the substituent on the arene offers steric control of the orientation of bridgehead N atoms, affecting their proton uptake and translocation ability. The heterogeneous electrochemical studies of these complexes physiadsorbed on edge plane graphite (EPG) electrode show the onset of HER activity at ∼180 mV overpotential in pH 5.5 water. In addition, bridgehead N-protonation and subsequent H-bonding capability are established to facilitate the O−O bond cleavage resulting in selective O_2 reduction to H_2O. This allows a synthetic [FeFe]-H_2ase model to reduce protons to H_2 unabated in the presence of dissolved O_2 in water at nearly neutral pH (pH 5.5); i.e., O_2-tolerant, stable HER activity is achieved.

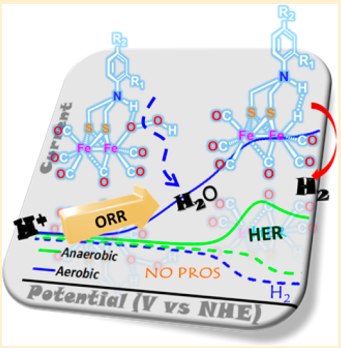

INTRODUCTION

The diiron [FeFe]-hydrogenase (H_2ase) is one of the two naturally occurring H_2ases that can catalyze the reduction of H^+ to H_2 reversibly.[1−3] The active site of the [FeFe]-H_2ase (H-cluster) contains a Fe_4S_4 cluster that is cysteine sulfur-linked to one of the iron centers (Fe_p) of a Fe_2S_2 subcluster (the 2Fe subsite), the redox active catalytic center (Scheme 1, center). An azadithiolato (ADT) bridge holds the two irons together in the 2Fe subsite; the geometry about the irons is completed with additional two cyanides and three carbonyl ligands. The consensus mechanism finds that the iron of the 2Fe subsite that is distal to the Fe_4S_4 cluster (Fe_d) directly interacts with H^+ or molecular H_2.[4,5] Recent spectroelectrochemical investigations under anaerobic conditions suggest that the Fe(I)Fe(I) state of the enzyme is responsible for binding the first added proton at the bridgehead nitrogen base.[6,7] Successive reduction and proton rearrangement results in a hydride-bound Fe(II)Fe(II)-H^- species (Scheme 1).[6] Further protonation occurs at the bridgehead amine, well positioned to couple with the hydride, to release H_2. The opposite direction is evoked for H_2 oxidation. The bridgehead nitrogen atom shuttles proton to and from the diiron active site;[8,9] ergo, the orientation of the nitrogen lone pair toward Fe_d is key to H_2ase activity.[10−13] The first reduction of the 2Fe subsite [Fe(I)Fe(I) state] is poised at −420 to −450 mV[13,14] at pH 7.0 where the enzyme operates with an overpotential (the additional energy needed above the thermodynamic potential of $H^+ + e^- = 1/2\ H_2$) of only 20−50 mV.[3] The turnover rates of [FeFe] H_2ase vary between 100 and 10000 s^{-1}.[3]

As the [FeFe]-H_2ases and their synthetic analogues are intolerant toward the presence of oxygen during catalytic turnovers, their utility as a practical water splitting agent is greatly compromised.[15−17] Hence, investigation of O_2 reactivities of H_2ases have emerged as an intense field of research. Initial EXAFS analysis with the enzyme suggested that reactive oxygen species (ROS), e.g., H_2O_2 and O_2^-, generated on O_2 exposure destroys the F_4S_4-cluster, rescinding the e^--shuttle and permanently damaging the HER activity (Scheme 2a).[18,19] Later, a theoretical investigation suggested that ROS may oxidize the Fe_4S_4, the 2Fe subsite, or any of the S atoms present in the H-cluster.[20−22] Studies of the electrocatalytic O_2 reduction with synthetic functional 2Fe subsite mimics have indicated that a large amount of ROS degrades the 2Fe subcluster models through S-oxygenation.[23] The major ROS responsible was proposed to be H_2O_2 resulting from the hydrolysis of a Fe(1.5)Fe(1.5)-OOH intermediate species involved in O_2 reduction by the Fe(I)Fe(0) state of these synthetic analogues (Scheme 2b).[23] The use of ROS scavenging additives like catalase, in the electrolytic solution, enhanced the catalytic turnovers for 2Fe

Received: June 7, 2018
Published: September 5, 2018

DOI: 10.1021/jacs.8b05983
J. Am. Chem. Soc. 2018, 140, 12457−12468

Scheme 1. Proposed Mechanistic Cycle of [FeFe]-H_2ase Enzyme, Adapted from Ref 6[a]

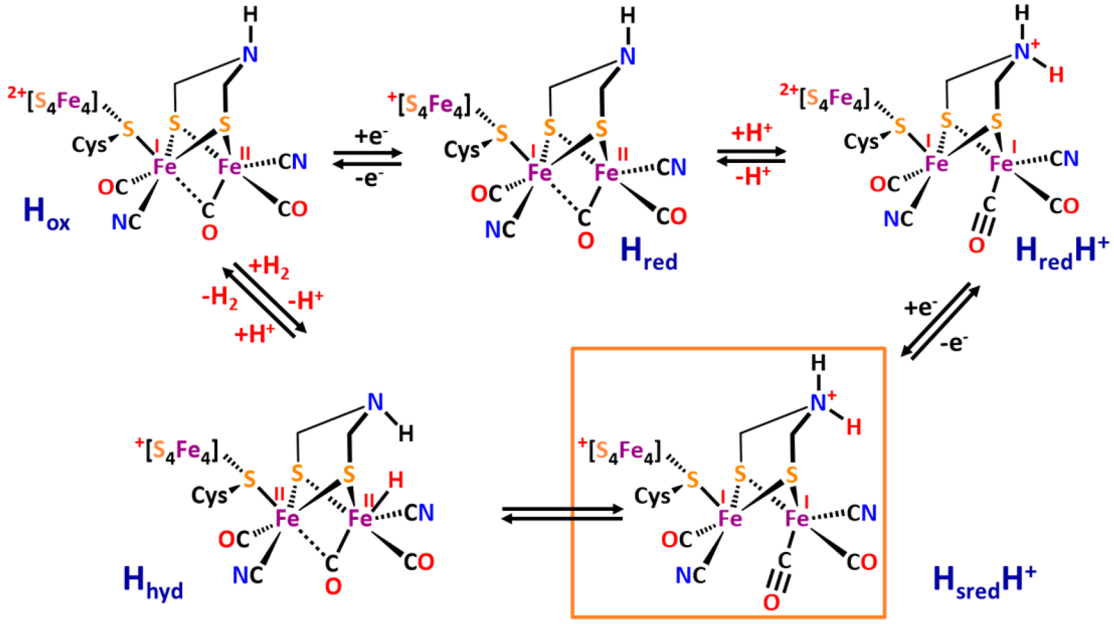

[a]The active site of the H-cluster is shown at the center. The formal oxidation states of the irons in the 2Fe subsite are indicated.

Scheme 2. Representative Schemes Summarizing O_2 Reactivities of H_2ases and Synthetic Models[a]

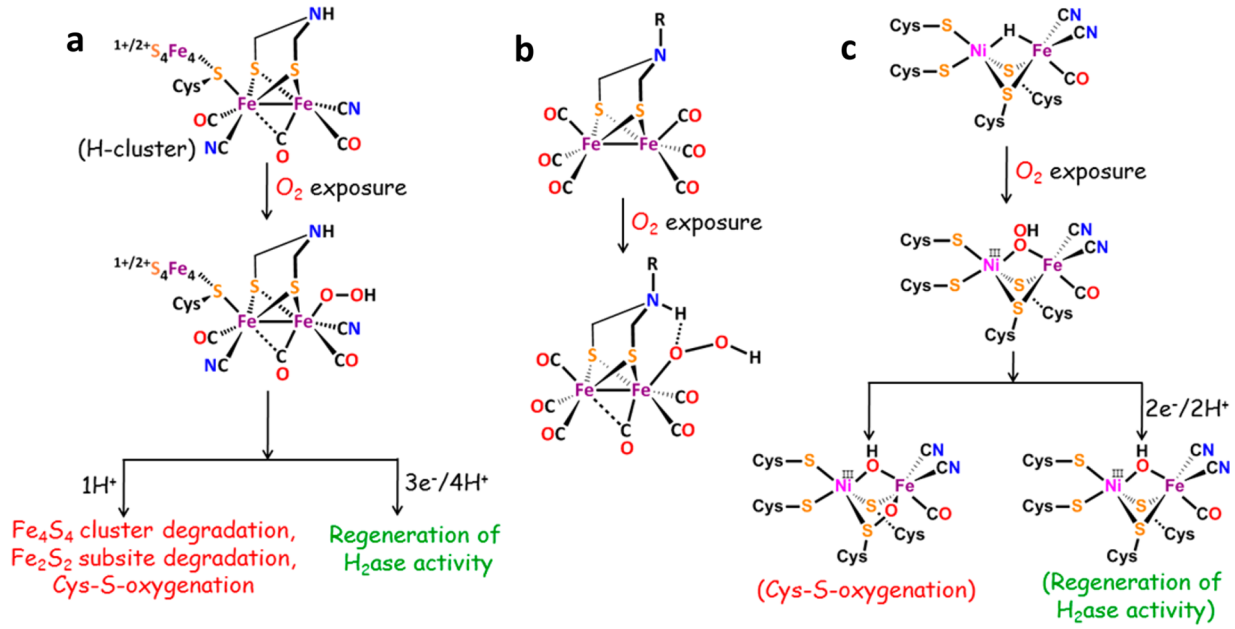

[a]In all schemes, the M−OOH is established as key reactive species for degradation. (a) The [FeFe]-H_2ase enzyme undergoes incomplete reduction to generate ROS and loses its activity; (b) in the case of [FeFe]-H_2ase models, the bridgehead N-protonation plays a key role in lowering the amount of ROS; and (c) the [NiFe]-H_2ase enzyme active site undergoes O_2 reduction in the Ni−C state to produce the Ni−(OOH)−Fe intermediate that oxidizes one of the Cys-S bridges to sulfenate ligand (Ni−B).

subsite mimics as well as other H_2 evolution catalysts.[23,24] Subsequent crystallographic investigations on enzymes demonstrated that indeed the 2Fe subcluster degrades first on O_2 exposure keeping the Fe_4S_4 cluster almost intact; activity could be reactivated through reinsertion of an intact 2Fe moiety.[25]

Initial experimental data on site-directed mutants show that the nearby Cys299 residue in the [FeFe]-H_2ase from *Chlamydomonas pastaurianum* (*Cp*) and Cys169 from *Chlamydomonas reinhardtii* (*Cr*) is oxidized to sulfenic acid (S−OH) by the ROS generated by the 2Fe subcluster in the presence of O_2.[26] Molecular dynamics calculations on the pathways leading to the generation of deleterious ROS in the enzyme active site suggested that reaction of molecular O_2 at the Fe_d site of Fe(II)−Fe(I) state and further reduction and protonation give an Fe(II)Fe(II)−OOH species that could either easily be released as H_2O_2 by taking a proton from adjacent Cys-SH or other reactive radical species.[26] Similar types of oxidative inactivation mechanisms were also

DOI: 10.1021/jacs.8b05983
J. Am. Chem. Soc. 2018, 140, 12457−12468

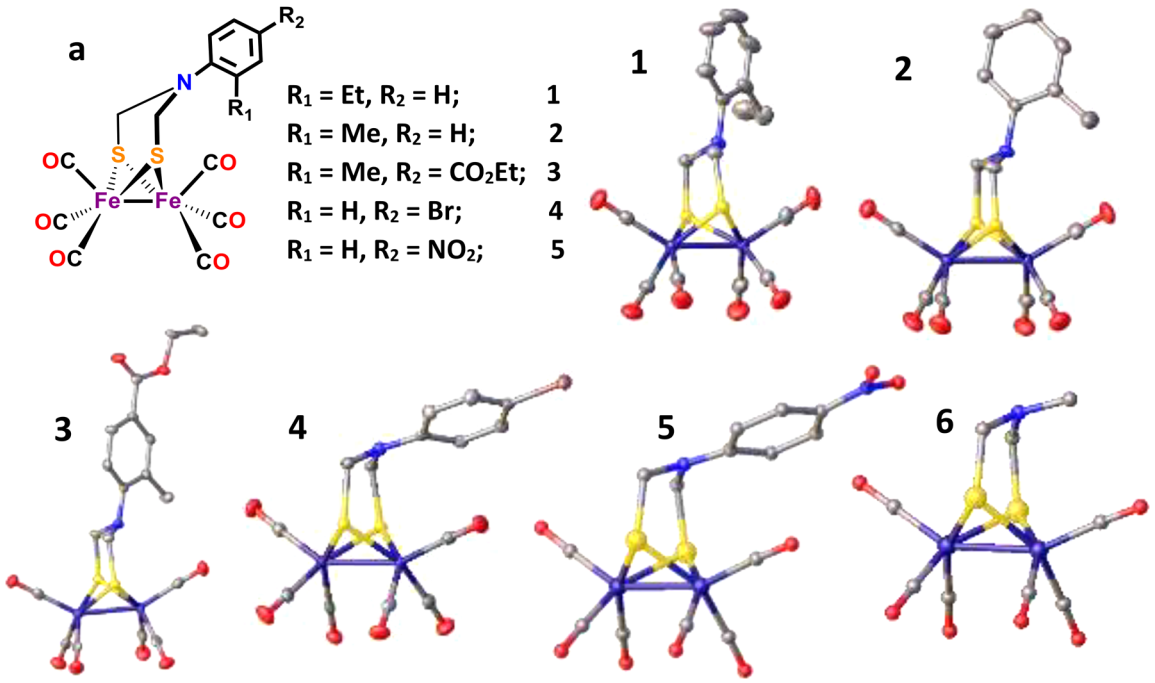

Figure 1. (a) Representative structures of the 2Fe subsite mimics of [FeFe]-H_2ases investigated in this report. Compounds **1**, **2**, **3**, **4**, and **5** are the XRD-determined structures of 2-ethyl, 2-methyl, 2-methyl-4-ethylethanoate, 4-bromo, and 4-nitro substituted phenyl amine containing ADT-bridged 2Fe subsite mimics, respectively. Compound **6** is the XRD-determined structure of N-Me substituted amine containing ADT-bridged 2Fe subsite mimic.

established for the [NiFe]-H_2ase enzyme. In this case, a Ni(III)−(OOH)−Fe(II) species (Scheme 2c), bearing resemblance to the Fe(II)Fe(II)−OOH species in [FeFe]-H_2ase, is formed on O_2 exposure, which immediately oxidizes the bridging thiolate ligand of the active site to sulfonate and generates the Ni-A (unready) state; the latter could be easily regenerated by reducing the sulfonates to thiol.[27] However, for [FeFe]-H_2ase, H-bonding between the cysteine thiol and the peroxide species was proposed to be important for stabilizing the Fe(II)Fe(II)−OOH intermediate and activating its O−O bond for cleavage, reducing the amount of ROS produced in the reaction of O_2 with the reduced active site.[26]

Similar hydrogen-bonding stabilization of such peroxide intermediates by an N-protonated ADT ligand was also suggested in synthetic analogues, which showed a 2-fold reduction of ROS produced from O_2 reduction at acidic, relative to neutral, pHs.[23] The protonation of the pendant amine group, only achieved at very low pHs, helped cleave the O−O bond and resulted in "partial" $4e^-/4H^+$ reduction of O_2 to benign H_2O offering the 2Fe cluster partial protection from ROS.[23] Recently, partial reversibility of the reaction of the reduced cluster with O_2 could be achieved and was ascribed to the rapid delivery of protons and electrons to the 2Fe subsite affecting $4e^-/4H^+$ reduction of O_2.[15,26,28,29] In [NiFe]-H_2ases oxygen tolerance is inherited from $4e^-/4H^+$ reduction of O_2 to benign H_2O.[27,30,31] Thus, results obtained from both H_2ase enzymes and synthetic analogues have hinted at the importance of a local proton source in affecting $4e^-/4H^+$ reduction of O_2 at the 2Fe active site, precluding the formation of ROS, which are responsible for irreversible damage to the 2Fe active site.

Through a biohybrid approach, i.e., the combination of synthetic analogues and apoenzyme from [FeFe]-H_2ase, the requirement for the bridgehead nitrogen in the ADT moiety has been unambiguously established.[10,32,33] The orientation of the nitrogen lone pair (N-*lp*) is also key for efficient heterolytic H−H bond formation or cleavage.[11,12] In fact, crystallographic evidence of a dihydrogen-bound intermediate has only been achieved for synthetic complexes where the orientation of the N-*lp* is directed toward the metal-hydride formation site.[12,34,35] While synthetic mimics of the Fe_2S_2 site are well explored,[36,37] only recently have promising electrocatalytic activities of these models been reported in aqueous environments.[38−40] Typically, these catalysts require substantial overpotentials and strongly acidic conditions to be functional. In comparison, of the synthetic catalysts, only those of Dubois work for overpotentials as low as 50−100 mV, albeit in organic solvents: their superior activity has been attributed to advantageous orientation of the basic moiety, which offers both thermodynamic and kinetic advantage to the HER process.[34,41−44] The importance of the bridging atom on the ADT in the HER reactivity of a 2Fe subcluster in physiologically relevant aqueous medium is yet to be demonstrated.

Our current study, with complexes physiadsorbed on EPG, demonstrates the remarkable effect of *o*-substitution on the geometry (through fixing the orientation of the N-*lp*) and reactivity of N-arylated, ADT-bridged synthetic mimics of [FeFe]-H_2ase Fe_2S_2 subsite (Figure 1: **1**, **2**, **3**). As **1**, **2**, and **3** complexes show HER activity in near-neutral pH (pH 5.5), complex **4**, having the N-*lp* delocalized into the aromatic ring, only works under very acidic conditions, and the advantage of directional N-*lp* in reducing the overpotential in electrochemical H−H bond formation is thus established. In addition, the basic and directed N-*lp* affects $4e^-/4H^+$ reduction of O_2 to H_2O and achieves the long sought after O_2-tolerant aerobic proton reduction in aqueous medium.

DOI: 10.1021/jacs.8b05983
J. Am. Chem. Soc. 2018, 140, 12457−12468

RESULTS AND ANALYSIS

Synthesis and Characterization. Complexes **1**, **2**, and **3** were synthesized by following a slightly modified literature procedure.[38,45] Generally, mixing of 2 equiv of *p*-formaldehyde with aromatic amines in CH_2Cl_2 for 3−4 h, followed by $SOCl_2$ addition, gives the bis-chloromethylated aromatic amine; condensation with the $Li_2(\mu\text{-}S)_2[Fe(CO)_3]_2$ salt in dry THF at low temperature leads to the target complex. The same protocol is followed for the *p*-bromoaniline and 4-nitroaniline, yielding **4** and **5**, respectively.[38,45−48] To obtain **1**, **2**, and **3** (**1** = *o*-Et aniline derivative; **2** = *o*-methyl; **3** = *o*-methyl-*p*-ethylcarboxylato), the reaction mixture must be stirred for 48 h (Figure 2, top). Although the bischloromethylated ligand was

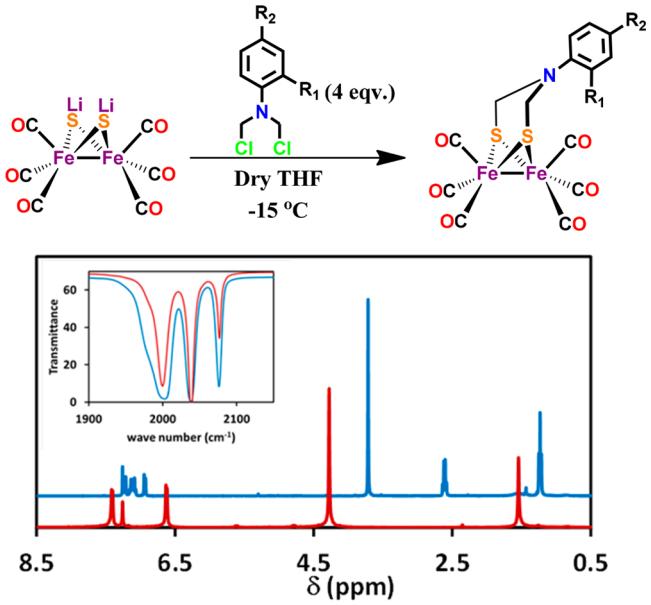

Figure 2. (top) General scheme for synthesis of 2-Et-Hyd (**1**), 2-Me-Hyd (**2**), and 3-methyl-4-aminobenzeneethanoate (**3**). (bottom) Overlay of ^{1}H NMR data of complex **1** (in sky blue) and complex **4** (in red). (inset) Overlay of FTIR data of the same complexes in acetonitrile solution.

isolated in analytically pure form as evident from the ^{1}H NMR data, the yields (37−48%) of **1**, **2**, and **3** are quite low compared to **4** and **5** (72−84%). The additional steric effect of *o*-substitution in the aromatic ring is the likely source of the lower yield. Nevertheless, **1**, **2**, and **3** show characteristic CO vibrations in the 2074 to 1997 cm^{-1} range in CH_3CN similarly to **4** and **5** (Table 1).[45,48]

The ^{1}H NMR spectrum of **1** in $CDCl_3$ shows very sharp signals (Figure 2, bottom, sky blue) suggesting that there is very little, if any, conformational flexibility in solution at RT. Furthermore, the CH_2 resonances are shifted upfield in complex **1** relative to complex **4** (Figure 2, bottom, red) directly implicating an increase in electron density on the $-CH_2-$ group of complex **1** suggestive of the diminishing conjugation of the adjacent bridgehead N-*lp* with the aromatic ring. Similar ^{1}H NMR spectra was also obtained for **2** and **3** (Figures S1 and S2). Hence, the *o*-substitution provides a framework that renders the N-*lp* conjugation with the aromatic ring.

Deep red needle-like X-ray quality single crystals could be obtained by slow evaporation of a CH_2Cl_2 solution of these complexes, and the X-ray crystallographic structures are displayed in Figure 1. The Fe−Fe, Fe−S, and Fe−CO bond lengths of complex **1**, **2**, and **3** are in the range reported for similar complexes in the literature, e.g., complex **4**, given in Table 1. Importantly, the crystal structures show that the dihedral angles defined by the C_2C_1 carbons of the aryl ring and the NC of the ADT ligand in complexes **1**, **2**, and **3** are ~80.5 ± 1.5° (Table 1, C−C−N−C), which are relatively large compared to only 6° in **4** and 2.89° in **5**. In sharp contrast to all known structures of *N*-aryl substituted ADT where the phenyl plane is almost coplanar with the C−N−C plane (Figure 3, right), the planes of the aromatic rings in complexes **1**, **2**, and **3** are rotated (Figure 3, green) substantially away from the C−N−C plane (Figure 3, red) of the ADT. The three C−N−C angles are 112°, 112°, and 113°. Thus, the N centers in complexes **1**, **2**, and **3** are tetrahedral suggesting a sp^3 hybridization at the N relative to a more planar geometry in other *N*-aryl substituted complexes. A greater basicity is thus expected for the nitrogens of **1**, **2**, and **3** since resonance delocalization of the nitrogen lone pair into the aromatic ring is operative in **4** and **5**. Hence, the high field shift in δ (ppm) values of **1** relative to **4** could easily be due to the loss of the delocalization of the N-*lp* in the aromatic ring. The increased electron density on the N atom in complexes **1**, **2**, and **3** is delocalized into the Fe_2S_2 cluster and results in minor, but perceptible, shifts in C−O vibrational frequencies in the FTIR in complex **1** (Figure 2 inset, sky blue) relative to those of complex **4** (Figure 2 inset, red), indicating increased electron density into the diiron unit and resulting in enhanced backbonding in **1**. It is also important to note that the direction of the N-*lp* of complexes **1**, **2**, and **3** toward one of the Fe's is considered key for efficient HER activity.[10,34]

Electrochemical Investigations. The cyclic voltammetry (CV) of complex **1** in CH_3CN (1 mM solution, scan rate of 20 mV/s, a glassy carbon (GC) working electrode, and 0.1 M nBu_4NClO_4 as supporting electrolyte) shows a quasi-reversible redox event at −1.55 V vs $Fc^{+/0}$, characteristic of these clusters (Figure 4, blue).[38,49−51] Complexes **2** and **3** also show similar behavior in CH_3CN solution (Figure 4, green and red, respectively). These complexes can be physiadsorbed on edge-plane graphite (EPG) electrodes allowing investigation of these modified electrodes in aqueous medium−an approach that was successfully applied for complex **4**.[38] X-ray photoelectron spectroscopy (XPS) of the EPG electrode bearing complex **1** shows ionization energies 710.9 and 724.8 eV corresponding to the ionization of the $2p_{1/2}$ and $2p_{3/2}$ levels of the Fe(I) canters, respectively. The peak centered at 399.8 eV represents the ionization of the tertiary amine nitrogen atoms, and the peak at 162.3 eV corresponds to the ionization of 2p of thiolate sulfur characteristic of these type of complexes (Figure S3).[52,53]

In an unbuffered aqueous solution containing 0.1 M KPF_6 (measured pH 5.5), a cathodic process at −50 mV and anodic process at 290 mV vs NHE (Figure 5a, blue) is assigned to the $\mathbf{1}/\mathbf{1}^-$ redox event (i.e., Fe(I)Fe(I) + e^- ⇌ Fe(0)Fe(I) redox process) where the reduced Fe(I)Fe(0) state has been reported to reduce O_2.[23] On sweeping the electrode potential further negative, another redox process associated with a Faradaic current is observed at −500 mV vs NHE (Figure 5b, blue). Very similar observations were also observed for **2** (Figure 5b, green) and **3** (Figure 5a,b, red) as well. These catalytic responses represent proton reduction by the Fe(0)-Fe(0) redox state at pH 5.5 with an onset potential of −500 mV. The onset potential is defined here by the substantial enhancement of the current with the complex-modified

DOI: 10.1021/jacs.8b05983
J. Am. Chem. Soc. 2018, 140, 12457−12468

Table 1. Geometric and Spectroscopic Comparison of Complexes 1, 2, 3, 4, 5 and 6 As Determined from X-ray Crystal Structure

complex	ν(CO) IR (cm^{-1})	bonds	average bond length (Å)	dihedral angle (C−C−N−C) (deg)
2-Et-Hyd (**1**)	2074, 2037, 1997	Fe−Fe	2.510 (±0.001)	80.90
		Fe−S	2.250 (±0.001)	
		Fe-CO	1.801 (±0.001)	
2-Me-Hyd (**2**)	2073, 2036, 1999	Fe−Fe	2.505 (±0.001)	80.90
		Fe−S	2.246 (±0.001)	
		Fe-CO	1.801 (±0.001)	
2-Me-4-carboxyethanoate-Hyd (**3**)	2074, 2038, 1998	Fe−Fe	2.489 (±0.001)	78.50
		Fe−S	2.252 (±0.001)	
		Fe-CO	1.794 (±0.001)	
4-Br-Hyd (**4**)	2076, 2040, 2000	Fe−Fe	2.497 (±0.001)	6.01
		Fe−S	2.257 (±0.001)	
		Fe-CO	1.795 (±0.001)	
4-NO_2-Hyd (**5**)	2075, 2039, 2000	Fe−Fe	2.507 (±0.001)	2.89
		Fe−S	2.266 (±0.001)	
		Fe-CO	1.801 (±0.001)	
N-Me-Hyd (**6**)	2074, 2037, 1996	Fe−Fe	2.492 (±0.001)	NA
		Fe−S	2.259 (±0.001)	
		Fe-CO	1.791 (±0.001)	

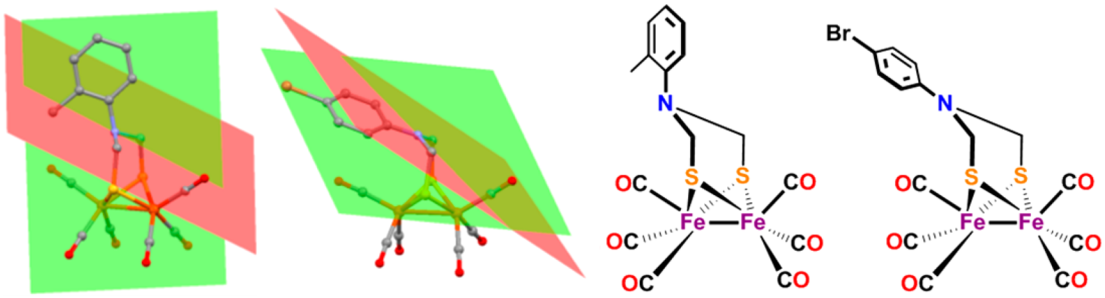

Figure 3. (left) Structures of complexes **2** and **4** showing the orientation of phenyl (in green) and the $-H_2C-N-CH_2-$ planes of the ADT (in red), 80.09° and 6.01°, respectively; (right) the chemical structures of **2** and **4**.

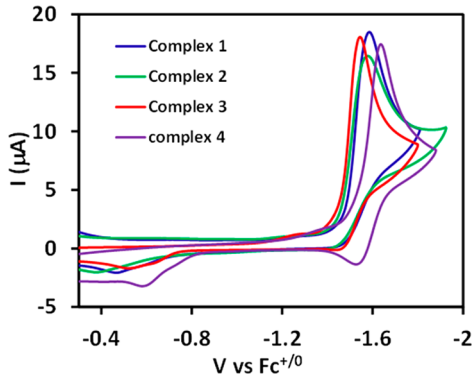

Figure 4. Homogeneous cyclic voltammetry of complexes **1**−**4** in ACN solution (1 mM solution, scan rate 20 mV/s, GC working electrode (diameter 3 mm) and Pt counter electrode, 0.1 M nBu_4NClO_4 supporting electrolyte).

electrode compared to the bare EPG electrode under the same condition. The large "(+)ve" shift in potential for these complexes was previously attributed to the greater aqueous solvation of the anionic species formed on reduction.[38] Note that the reduction potentials of complexes **1**, **2**, **3**, and **4** are very similar in both organic and aqueous solutions. Thus, the HER observed at low overpotentials in the *ortho*-substituted derivatives strongly implicates a role for the N-*lp* in these.

Product Analysis and Catalytic Parameters. To establish the nature of the Faradaic process at −500 mV vs NHE, rotating ring disc electrochemistry (RRDE) was performed to enable *in situ* product analysis.[54] All the potentials for the heterogeneous electrochemistry is reported vs NHE as they are recorded using water as electrolytic medium. In an RRDE experiment, any H_2 produced at the working electrode bearing these complexes diffuses as a result of the hydrodynamic force created on rotation of the shaft holding the EPG working electrode; the H_2 produced is concomitantly detected at a Pt ring (secondary electrode, poised at a constant potential of 0.5 V) encircling the working EPG electrode, where the H_2 is reoxidized to H^+ (Figure 5c).[36] This technique is very widely used for various catalytic processes associated in energy transduction processes. Indeed, a RRDE experiment using a EPG electrode modified with **1** shows detection of H_2 at the Pt ring (Figure 5c, purple) with an onset potential of −500 mV under anaerobic condition. The overpotentials (η) for HER (determined by $E^0_\eta = -0.059 \times pH - E_{onset}$) is ∼180 mV for complex **1** (Figure S4; **2** and **3** are given in the SI) at pH 5.5; this value is considerably lower than other [FeFe]-H_2ase mimics investigated in aqueous medium. The corresponding Tafel plot of the electrochemical polarography also shows a similar overpotential (Figure S5). Bulk electrolysis (BE) at −700 mV with glassy carbon counter electrode results in a steady current (Figure 5b and a comparison with Pt counter in Figure S6 left) indicating that

DOI: 10.1021/jacs.8b05983
J. Am. Chem. Soc. 2018, 140, 12457−12468

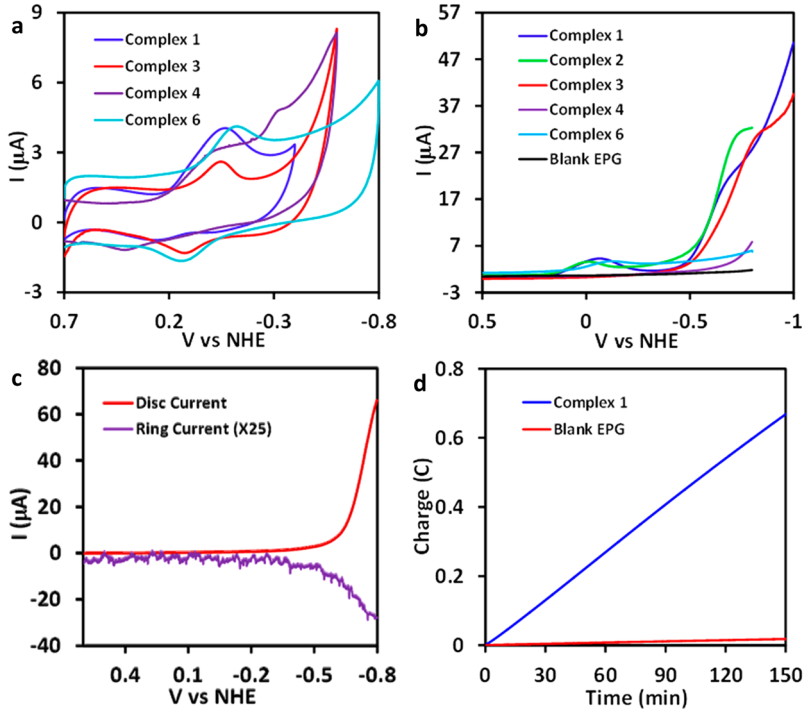

Figure 5. (a) Overlay of cyclic voltammetry (CV) data of complexes **1**, **3**, **4**, and **6** physiadsorbed on EPG surface in KPF_6 solution (pH 5.5) on different potential range (scan rate 50 mV/s). (b) Overlay of linear sweep voltammetry data in KPF_6 solution (scan rate: 50 mV/s). (c) RRDE data of **1** on EPG electrode in KPF_6 solution; red line indicates H_2 generation and violet line represents the H_2 oxidation at the Pt ring. The ring was held at a constant potential of 0.5 V. The Pt current is enhanced 25×. (d) Controlled potential bulk electrolysis at −0.7 V in aqueous KPF_6 solution of complex **1** (blue) with GC counter electrode and blank EPG (red).

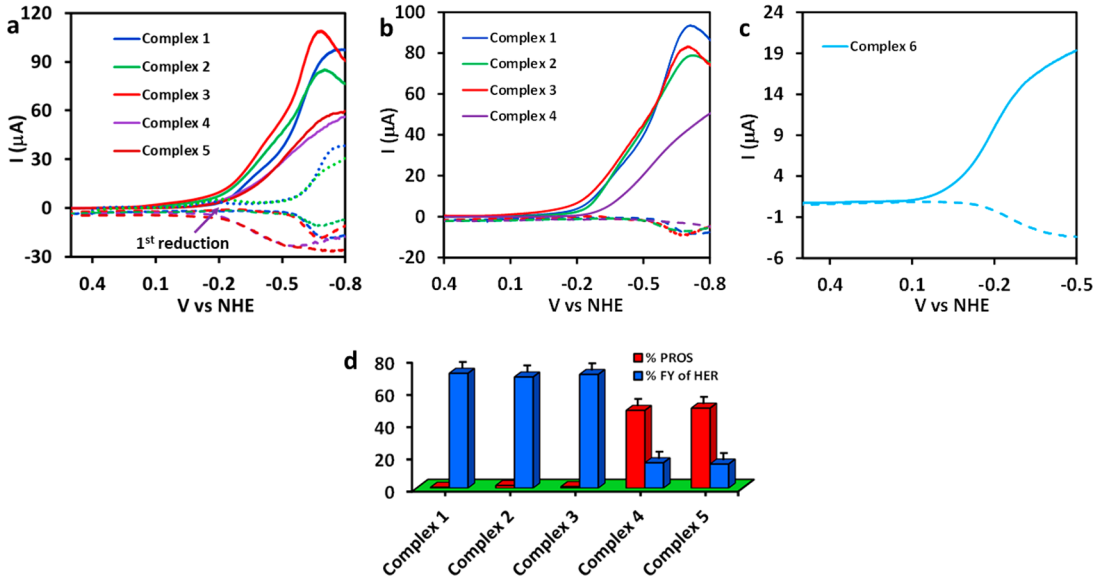

Figure 6. (a) Overlay of aerobic RRDE responses of complexes **1**−**5**, holding the Pt ring at 0.70 V. Scan rate 50 mV/s at pH 5.5 (KPF_6 solution and 300 rpm). The "dashed line" represents the corresponding Pt-ring current. The "dotted line" is the LSV of complexes **1** and **2** under anaerobic condition and with the electrodes held static. (b) Overlay of aerobic RRDE data for complexes **1**−**4**, holding the Pt ring at 0.5 V. Scan rate 50 mV/s at pH 5.5 (KPF_6 solution). The Pt ring current is multiplied by a factor of 15 for all complexes in panel b. However, in panel a, the multiplication factor is 15 for **1**, **2**, and **3** and 10 for **4** and **5**. (c) Overlay of aerobic RRDE responses of complex **6**, holding the Pt ring at 0.70 V. Scan rate 50 mV/s at pH 5 phosphate buffer. The Pt ring current is multiplied by a factor of 2 in panel c. (d) Bar diagram of % PROS and % FY of HER for complexes **1**−**5**.

1 is stable under these conditions, and the gas collected is confirmed as H_2 using gas chromatography (GC) fitted with a thermal conductivity detector (TCD) (Figure S7). The overall faradaic yield (which is a direct measure of the charge converted to product) obtained as a ratio of H_2 gas collected to the charge dispensed during BE is >95 ± 2%. The TOF_{max} of the catalysis is determined from the I_{cat}/I_p ratio at room temperature, which is a convenient way of describing the

DOI: 10.1021/jacs.8b05983
J. Am. Chem. Soc. 2018, 140, 12457−12468

catalytic efficiency for heterogeneous electrocatalysts;[55,56] it is calculated to be 13.3 and 40.1 s^{-1} at −600 mV and −800 mV vs NHE, respectively. The TOF_{max} was also determined for complexes **2** and **3** and lies within 11.2−15.4 s^{-1} at −600 mV and 32.2−49.4 s^{-1} at −800 mV. The TON of complex **1** for HER is determined from bulk electrolysis data obtained at −700 mV for 10 h to be $\gg 10^6$ (SI, page S9). Similar results were also obtained for **2** and **3**.

It has been earlier reported that the complexes within this series are quite stable as catalysts for electrocatalytic HER.[38] Previous reports on a [FeFe]-H_2ase mimic−SDS composite show I_{cat}/I_p value <3 s^{-1} at near-neutral pH (pH 5.5),[40] while the rest of the H_2ase mimics show HER activity at much lower pHs.[38,39] Post electrolysis surface analysis of the modified EPG by XPS show that the characteristic ionization energies remain almost unaltered during bulk electrolysis (Figure S8). Hence, the HER activity originates from the molecular complex **1**. Complex **1** shows substantial higher activity (Figure 5b, blue line) compared to complex **4** (Figure 5b, purple line) at near-neutral pH. Note that complex **4** is known to be a facile HER catalyst in acidic solution with 500 mV overpotentials; however, it has almost no activity at pH 5.5 (Figure 5b), whereas complex **1** is very active.[38] A very similar trend is observed for complexes **2** and **3** for HER (Figure 5b, green and red). The results suggest that the high activity of **1**, **2**, and **3** are due to the presence of the well-oriented N-*lp* with higher pK_a adjacent to the proton binding site. The N-*lp* may either assist protonation at higher pHs or may facilitate the formation of the H−H bond by retaining a proton in the vicinity of a Fe−H species formed after the initial protonation and electron transfer from the cluster.

Oxygen Reduction and Aerobic H_2 Production. In a previous report, we suggested that bridgehead N-protonation may lead to the facile O−O bond cleavage resulting in $4e^-/4H^+$ reduction of O_2 to benign water; ergo, lower amounts of ROS, which is also known as PROS (partially reduced oxygen species, as generated under electrolytic condition through insufficient transfer of electron to molecular oxygen), produced during competitive O_2 reduction by [FeFe]-H_2ase models under aerobic conditions. In the *N*-aryl bridged models, where the pK_a of the nitrogen is quite low, a smaller amount of ROS from O_2 reduction could only be observed at pH < 1.[23] The increased basicity of complexes **1**, **2**, and **3**, as evident from HER at near-neutral pH, may allow facile $4e^-/4H^+$ reduction of O_2 offering air stable HER reactivity. The RRDE scan with a complex **1**-modified EPG electrode (Figure 6a, blue line) showed two catalytic responses with −150 and −550 mV onset potential, respectively, in aerobic electrolytic solution (pH 5.5, KPF_6 solution). The first catalytic process overlays with the Fe(I)Fe(I)/Fe(I)Fe(0) process, whereas the second catalytic process overlays with the HER response of **1**, **2**, and **3** and corresponds to the Fe(I)Fe(0)/Fe(0)Fe(0) process. Previous work by this group showed that electrocatalytic O_2 reduction by synthetic mimics of [FeFe]-H_2ase develops at the Fe(I)Fe(I)/Fe(I)Fe(0) state.[23] Accordingly, the first catalytic process is the electrocatalytic oxygen reduction, and the second catalytic process will have contributions from HER and, possibly, ORR catalyzed by the Fe(0)Fe(0) state.

Rotating ring disc electrochemistry (RRDE) is a convenient technique to analyze the individual products of these two catalytic processes, H^+ and/or O_2 reduction (Figure 6a,b). If the Pt ring is held at a fixed potential of 0.5 V, it can oxidize H_2, the product of HER, whereas holding it above 0.7 V permits detection of both H_2 and any ROS produced during O_2 reduction. Holding the Pt ring at 0.5 V showed no current for the first catalytic process, whereas a H_2 oxidation current was observed during the second catalytic process at −0.52 V for **1**, **2**, and **3** due to H_2 formed from HER (Figure 6b). Holding the potential of the ring at 0.7 V shows no current corresponding to the ORR at −0.15 V from complexes **1**, **2**, and **3**, indicating no ROS production during O_2 reduction (Figure 6a). On the contrary, complexes **4** and **5**, without the *ortho* substituents, show a large Pt ring current corresponding to the O_2 reduction process at −0.15 V, indicating generation of a large amount (∼50%) of ROS during O_2 reduction (Figure 6a). Similarly, complex **6** also shows a large amount of ROS (∼50%) at pH 5 phosphate buffer when the Pt ring is held at a potential of 0.7 V (Figure 6c). These results unambiguously demonstrate that complexes **1**, **2**, and **3** efficiently reduce O_2 by $4e^-/4H^+$ to H_2O with high selectivity; however, complexes **4**, **5**, and **6** produces ∼50% H_2O_2 under the same conditions.

The ROS produced by complexes **4**, **5**, and **6** on reaction with O_2 in their reduced states results in the oxidation of the bridging thiolate ligands leading to degradation of the 2Fe cluster.[23] The lack of ROS during O_2 reduction by complexes **1**, **2**, and **3**, due to $4e^-/4H^+$ reduction of O_2 to water, raises the possibility of stable HER by these complexes in the presence of O_2. To check the stability and aerobic HER activity, bulk electrolysis using **1** was performed at −700 mV, under aerobic conditions for hours with GC counter as well as Pt counter electrode. The results do not show any loss in the HER activity at least over a few hours (Figure S9). The % of Faradaic yield (FY) of aerobic HER is estimated to be ∼70% for complex **1**−**3**. Postelectrolysis analysis of the electrode by XPS shows that the complexes do not degrade much, even under aerobic electrolysis time courses (Figure S10). We presented the % FY and % PROS for complexes **1**−**5** as a bar diagram in Figure 6d. The results suggest that diminishing the amount of PROS for complexes **1**−**3** enhances the stability as well as FY for HER in the presence of O_2. However, complexes **4** and **5** show competitive $2e^-/2H^+$ ORR resulting in PROS, leading to faster degradation of these complexes. The average $TOF_{aerobic}$ can be calculated from aerobic bulk electrolysis data (Figure 5d), and the values are determined to be 16.2−23.1 s^{-1} for complexes **1**−**3** in the presence of oxygen. Spectrometric quantification of the ROS generated, by Xylenol orange assay, was done with the electrolytic solution after BE, and the results suggest that only a small amount of ROS is generated over 10 h of BE (SI, page S13). Postaerobic bulk electrolysis XPS analysis of the modified EPG electrode shows the retention of the characteristic ionization peaks of complex **1** on the electrode surface (Figure S10). The ATR-IR spectra of the modified EPG electrode before and after aerobic bulk electrolysis of complex **1** show no changes of the CO vibrations (Figure S11). Thus, rotation of the phenyl ring off resonance due to the *ortho* substitution not only allows HER at near-neutral pH with low overpotential but also affects $4e^-/4H^+$ reduction of O_2 allowing oxygen-tolerant HER. These results strongly corroborate the findings in both [FeFe]- and [NiFe]-H_2ases where a sufficient or excess supply of electrons and a local proton relay allows selective $4e^-/4H^+$ reduction of O_2 to benign H_2O, precluding the formation of harmful reactive oxygen species (ROS), affecting oxygen-tolerant HER.

To corroborate the O_2 reduction ability of a working proton-reduction catalyst, the experiment described in Figure 7 was

DOI: 10.1021/jacs.8b05983
J. Am. Chem. Soc. 2018, 140, 12457−12468

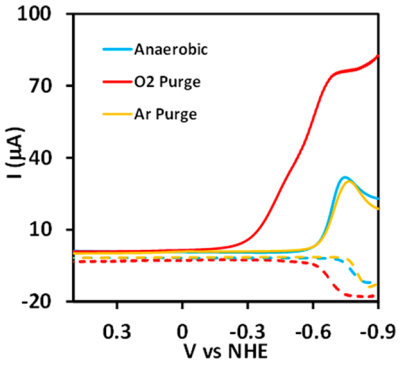

Figure 7. Overlay of RRDE of complex **1** in different conditions. The cyan is RRDE in anaerobic condition, the red one is the RRDE in O_2 purge condition, and the yellow one is the RRDE in Ar purge condition. During anaerobic (sky blue) and Ar purge (yellow) conditions, the Pt ring was held at 0.5 V. In the case of O_2 purge condition (red), Pt ring was held at 0.7 V. "Dashed line" indicates the corresponding Pt ring current scaled by 25.

carried out. Here, the HER activity of complex **1** at pH 5.5 in a degassed electrolyte solution (Figure 7, cyan) is overwhelmed by ORR current when the electrolytic solution is saturated with O_2 (Figure 7, red). The retained HER activity under these circumstances is evidenced by the H_2 detection current at the Pt ring (Figure 7, dashed cyan and dashed red for degassed and aerobic, respectively). On removing the dissolved O_2 by purging with Ar gas, the ORR electrocatalytic activity is lost, and the original HER activity is reinstated (Figure 7, yellow, and H_2 detection, dashed yellow) thereby emphasizing the oxygen tolerant HER catalyzed by these complexes.

DFT Calculations. The experimental results indicate that complexes **1** and **2** show selective $4e^-/4H^+$ reduction of O_2 to H_2O at near-neutral pH, whereas complexes **4** and **6** show substantial ROS at these pHs. Previous calculations of the reaction of the Fe(I)Fe(0) state with O_2 had identified that a putative Fe(1.5)Fe(1.5)−OOH species is responsible for the hydrolytic release of H_2O_2.[23] The cleavage of the O−O bond in this Fe(1.5)Fe(1.5)−OOH species results in $4e^-/4H^+$ reduction of O_2 (Figure 8). Thus, the experimental data suggests that the presence of the pendant protonated amines in **1** and **2** lowers hydrolysis and activates the O−O bond for cleavage. Recent investigations using iron porphyrins have revealed that the selectivity for $4e^-/4H^+$ reduction of O_2 can be enhanced by (a) activation of the O−O bond of a peroxide intermediate and (b) stabilization of the bound peroxide against hydrolysis via H-bonding.[57,58] In the absence of direct spectroscopic data on such species, geometry-optimized density functional theory calculations are utilized to provide insight.

The optimized structures of a putative Fe(1.5)Fe(1.5)−OOH intermediate for complexes **1**, **2**, **4**, and **6** (Figure 9) show that the protonated amine is hydrogen-bonded to the proximal oxygen of the terminal hydroperoxide ligand. The gas phase proton affinities (PA, Fe(I)Fe(I) state) for complexes **1**, **2**, and **6** relative to complex **4** are calculated to be −21, −20, and −16 kcal/mol, respectively, suggesting that the protonation of the amine in complexes **1** and **2** are likely to occur at higher pHs relative to complexes **4** and **6**. The calculated Fe−O stretching frequencies (ν_{Fe-O}; Table 2, Figure 9) in the optimized Fe(1.5)Fe(1.5)−OOH structures are higher for complexes **1** and **2** relative to **4** and **6** (Table 2). The stronger Fe−O bonds in the hydroperoxide adducts of complexes **1** and **2** are complemented by weaker O−O bonds (ν_{O-O}, Table 2).

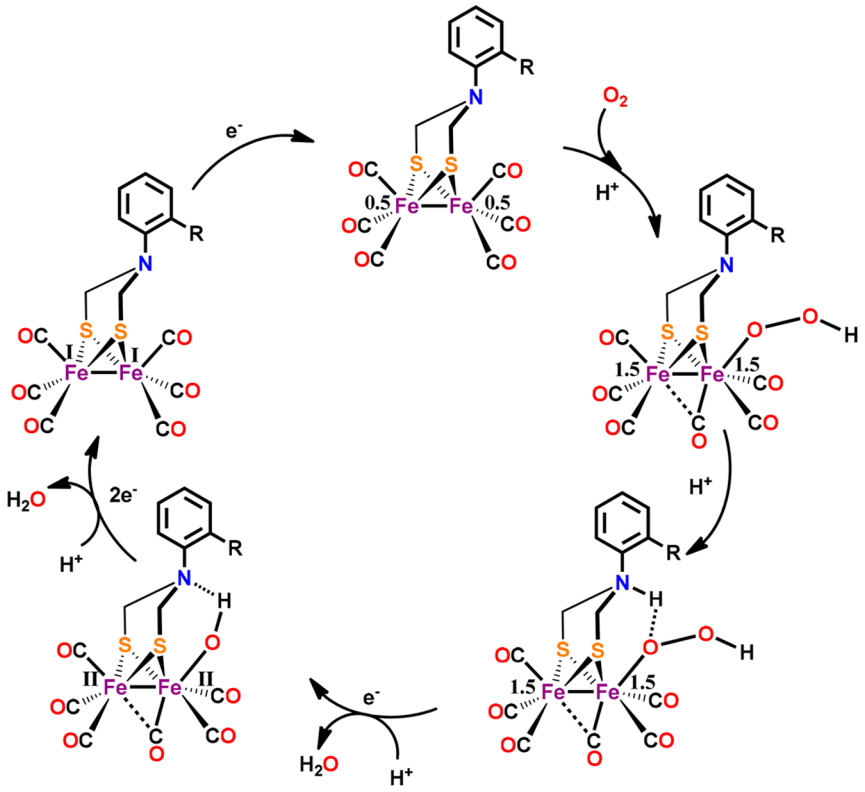

Figure 8. Proposed mechanistic scheme for O_2 reduction by *ortho*-substituted ADT-bridged [FeFe]-H_2ase mimics.[23]

DOI: 10.1021/jacs.8b05983
J. Am. Chem. Soc. 2018, 140, 12457−12468

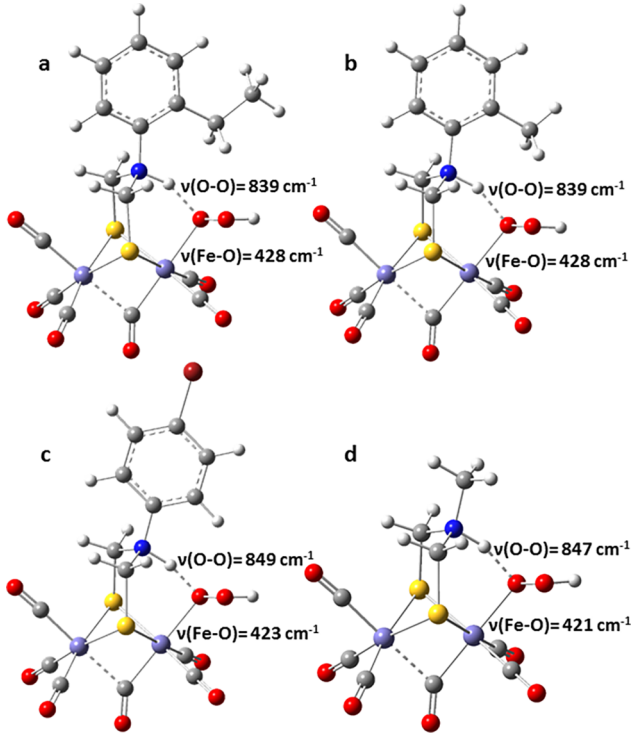

Figure 9. DFT-optimized hydroperoxide intermediate structures of (a) complex **1**, (b) complex **2**, (c) complex **4**, and (d) complex **6**.

Table 2. Fe−O and O−O Stretching Frequency and Bond Length of Different Complexes Determined from the DFT Optimized Structures

complexes	νFe−O (cm^{-1})	νO−O (cm^{-1})	Fe−O (Å)	ΔG (kcal/mol) H_2O_2 release	ΔPA (kcal/mmol)
1	428	839	1.996	4.67	−21
2	428	839	1.997	4.66	−20
4	423	849	2.014	0	0
6	421	847	2.005	9.03	−16

The ΔG of hydrolysis of H_2O_2 from the Fe(1.5)Fe(1.5)−OOH species is uphill in complexes **1**, **2**, and **6** relative to complex **4** (Table 2). Thus, the DFT calculations suggest stabilization of the labile hydroperoxide (higher ΔG hydrolysis) group and activation of its O−O (weaker ν_{O-O}) bond by hydrogen bonding by the pendant basic group consistent with selective $4e^-/4H^+$ reduction of O_2 by complexes **1** and **2** at higher pH (higher PA). While complex **6** shows stabilization of the bound hydroperoxide by hydrogen bonding, the hydroperoxide ligand is not activated for O−O cleavage (strong ν_{O-O}) relative to complex **4**. As a result, the activation barrier for O−O bond cleavage is likely higher in complex **6**, which produces substantial H_2O_2 ($2e^-/2H^+$ product) relative to complexes **1** and **2**.

CONCLUSION

In summary, *ortho* substitution of the aryl groups in *N*-aryl-substituted ADT-bridged dithiolate in synthetic mimics of the 2Fe subsite of H_2ase induces pyramidality at the bridgehead nitrogen that appears to foster the ability of these complexes to reduce protons in the presence of oxygen at near-neutral pH with low overpotential. The *ortho* substitution does not affect the formal reduction potentials of the complexes (active Fe(0)Fe(0) state at ∼−550 mV vs NHE); rather, it results in rotation of the phenyl ring rescinding resonance delocalization of the N-*lp* into the ring. The increased electron density at the well-oriented, pyramidal nitrogen allows protonation at near-neutral pH in contrast to unsubstituted *N*-aryl derivatives, which show HER only at pH < 1. Thus, despite having very similar formal potentials, the presence of an active local proton relay at higher pH (pH 5.5) allows HER at −500 mV vs NHE, much closer to the thermodynamic $H^+ + e^- \leftrightarrow 1/2\ H_2$ potential at that pH resulting in very low overpotentials for HER. The same proton relay allows the unprecedented selective $4e^-/4H^+$ reduction of O_2 to benign H_2O by these synthetic 2Fe models at neutral pHs when their predecessor, without the *ortho* substituent, produces >50% detrimental H_2O_2. Thus, emulation of the second sphere interactions, deemed important for O_2 tolerance in H_2ases, in synthetic complexes, proffers unprecedented O_2 tolerant, bioinspired HER catalysts that work efficiently at near-neutral pH. The highly versatile diiron complex, with its manifold of subtle tuning capabilities has shown in this study that the electrophilicity of O_2 is similar to that of the proton, and the reactive site for proton binding and reduction equally well competes for O_2 binding and reduction.[59]

EXPERIMENTAL SECTION

General Procedure. Syntheses of all the compounds were performed either under anaerobic atmosphere or in an Ar glove box from MBRAUN. Complexes **1** and **2** were synthesized using standard Schlenk techniques. 2-Methylaniline, 2-ethylaniline, and the solvents were used fresh after distillation. Thionyl chloride ($SOCl_2$) was purchased from Spectrochem Pvt. Ltd. (India), *p*-formaldehyde and superhydride ($Li[HBEt_3]$, 1 M in THF) were from Sigma-Aldrich Chemicals Pvt. Ltd., and anhydrous Na_2SO_4 and sulfuric acid (98%) were purchased from Merck Specialties, Pvt. Ltd. (India). Silica (60−120 mesh), for column chromatography, was purchased from SISCO Pvt. Ltd. (India). Edge plane graphite (EPG) discs were purchased from Pine Instruments. The FT-IR data are measured on the PerkinElmer FTIR Frontier instrument. All the NMR spectra were recorded on a Bruker DPX-400 or DPX-500 spectrometer at room temperature. The mass spectra were recorded on an QTOF Micro YA263 instrument. The H_2 gas from controlled potentiometry proton reduction was detected on a GC instrument of model no. 7890B (G3440B), serial no. CN14333203 fitted with a thermal conductivity detector (TCD).

General Procedures for Synthesis. *Complex 1, [(μ-SCH$_2$)$_2$N(2-Ethylphenyl)CH$_2$S)[Fe(CO)$_3$]$_2$.* Complex **1** was synthesized using standard Schlenk techniques by slightly modifying the synthetic protocol described in the literature.[45] To a solution of 2-ethylaniline (1.23 mL, 10 mmol), paraformaldehyde (780 mg, 26 mmol) was added; the solution was stirred for 2 days at room temperature. Then $SOCl_2$ was slowly added at 0 °C, and the mixture was brought to RT with stirring. After half an hour the solvent was evaporated completely to dryness to remove all the acid vapor. A 440 mg sample of $(\mu\text{-}S_2)[Fe(CO)_3]_2$ (1 mmol) was dissolved in 20 mL of dry tetrahydrofuran (THF). Two milliliters of $LiBEt_3H$ (1 M in THF) was added dropwise to the red solution at −78 °C, with immediate color change to deep green. Following cooling to −15 °C, a THF solution of the ligand 2-Et$C_6H_4N(CH_2)_2Cl_2$ (4 equiv) was added to the reaction mixture. The color immediately changed to red. The reaction mixture was further stirred for 1 h at RT. Vacuum removal of the solvent produced a dark brown precipitate. A crystalline red solid product was obtained after column chromatography with a hexane−toluene (9:1) mixture. Single crystals were grown by slow evaporation of a CH_2Cl_2 solution of the complex. Overall yield: 41%. ^{1}H NMR ($CDCl_3$, 400 MHz): δ 7.22 (J = 7.2, 1H, d), 7.12 (2H, m), 6.94 (J = 7.6, 1H, d), 3.72 (s, 4H), 2.61 (J = 7.466, 2H, quar), 1.23 (J = 7.6, 3H, t). IR (CH_3CN): 2074 cm^{-1}(s), 2037 cm^{-1}(s), 1997 cm^{-1}(s). ESI-MS data $(M + H)^+$ = 497.9379 (m/z). Elemental Analysis

DOI: 10.1021/jacs.8b05983
J. Am. Chem. Soc. 2018, 140, 12457−12468

(found): C, 38.28; H, 3.81; N, 2.65; calculated C, 38.65; H, 3.85; N, 2.82.

Complex 2, [(μ-SCH$_2$)$_2$N(2-Methylphenyl)CH$_2$S)[Fe(CO)$_3$]$_2$. Complex **2** was synthesized following the exact same procedure described for **1**, using 2-methylaniline instead of 2-ethylaniline. The column chromatography was performed using a hexane−toluene (9:1) mixture. Suitable single crystals were obtained by slow evaporation of a CH_2Cl_2 solution of the complex. Overall yield is 35%. ^{1}H NMR ($CDCl_3$): δ 7.25 (1H, d), 7.14 (2H, m), 6.94 (1H, d), 3.71 (s, 4H), 2.60 (3H, s). IR (CH_3CN): 2073 cm^{-1} (s), 2038 cm^{-1} (s), 1999 cm^{-1} (s). ESI-MS data $(M + H)^+$ = 483.9214 (m/z). Elemental Analysis (found): C, 37.34; H, 3.79; N, 2.42; calculated C, 37.29; H, 3.55; N, 2.90.

Complex 3, [(μ-SCH$_2$)$_2$N(2-Methyl-4-carboxyethanoate-phenyl)-CH$_2$S)[Fe(CO)$_3$]$_2$. Complex **3** was synthesized exactly following the same procedures described for **1** and **2**, using 3-methyl-4-amino-benzeneethanoate (details of ligand synthesis are in the SI). The column chromatography was performed with a hexane−CH_2Cl_2 (4:1) mixture. Suitable single crystals were obtained by slow evaporation of a CH_2Cl_2 solution of the complex. The overall yield is 49%. ^{1}H NMR ($CDCl_3$): δ 7.83 (1H, s), 7.81 (1H, s), 6.94 (1H, d), 4.34 (2H, quart), 3.94 (s, 4H), 2.28 (3H, s), 1.38 (3H, t). IR (CH_3CN): 2075 cm^{-1}(s), 2037 cm^{-1}(s), 1999 cm^{-1} (s). ESI-MS data $(M+H)^+$ = 555.957 (m/z). Elemental Analysis (found): C, 38.67; H, 3.96; N, 2.49; calculated C, 38.94; H, 3.81; N, 2.52.

Electrochemical Measurements. All the electrochemical experiments were performed using a CH Instruments (model CHI 710D) Electrochemical Analyzer. Reference electrodes and Teflon plate material evaluating cell (ALS Japan) were purchased from CH Instruments. The rotating ring disk electrochemical (RRDE) set up from Pine Research Instrumentation (E6 series Change Disk tips with AFE6M rotor) was used to obtain the RRDE and LSV data. A Pt wire was used as a counter electrode. All the measurements were performed against Ag/AgCl aqueous leak-proof reference electrode (satd. KCl). In the case of aqueous measurements, the potentials were converted to NHE by adding 200 mV with the value obtained by using Ag/AgCl (satd. KCl). Anaerobic CV experiments were performed in a glove box filled with N_2 or within a five-neck S3 water jacketed electrochemical cell (PINE Instruments) by thoroughly degassing the whole set up with Ar gas. Particulars of various electrochemical techniques are given in successive sections.

Homogeneous CV. A glassy carbon electrode and a Pt wire were the working and the counter electroded, respectively. The measurements were done against aqueous Ag/AgCl reference electrode (satd. KCl) and corrected to $Fc^{+/0}$. Homogeneous CV experiments were performed with 1 mM solution of any complex and 0.1 M [n-Bu_4N][ClO_4] in CH_3CN in a glove box at RT. The working glassy carbon electrode was polished and washed well before each single experiment.

Construction of Graphite Electrodes. The edge plane graphite (EPG) electrode was freshly polished and cleaned with polishing kit before each single experimental use. A 200 μL portion of a dilute solution (∼1 mM, in CH_2Cl_2) was uniformly dropcasted on the cleaned EPG disc (5 mm outer diameter) fitted within a shaft. After the CH_2Cl_2 was evaporated, the surface was washed with $CHCl_3$ thoroughly and sonicated in ethanol to remove any loosely bound catalyst on the surface and washed with triple distilled water.

Heterogeneous CV. The aqueous cyclic voltammogram was recorded with the same instrument and same software in 0.1 M KPF_6 water solution with all of the complexes adsorbed onto the EPG disc (5 mm outer diameter) held within a shaft (Pine Instruments, AFE6MB). An anaerobic environment was maintained within a water jacketed electrochemical cell (Pine Instrument, RRPG138) by purging with Ar gas for 1 h. The aqueous Ag/AgCl reference (Pine instruments, RREF0021) and Pt counter (AFCTR5) electrodes were attached to the cell through airtight joints.

Rotating Disc Electrochemistry. The RDE/RRDE measurements were performed in a CHI 710D or 720D bipotentiostat. An EPG disc was used as the working electrode, which was mounted inside of a Pt ring assembly (Pine Instrument, AFE6RIP), itself mounted at the tip of a shaft (Pine Instruments, AFE6MB), which in turn was fitted to a MRS rotator. A water jacketed electrochemical cell (Pine Instrument, RRPG138) is used where the rotor was inserted through a taper plug assembly (AC01TPA6M), which allows free rotation of the vertical rotor while maintaining an airtight seal. An aqueous Ag/AgCl reference (Pine instruments, RREF0021) and Pt counter (AFCTR5) electrodes are attached to the cell through airtight joints. The EPG fitted shaft is then tethered just before the experiment is begun.

Electrochemical Hydrogen Production. The shaft bearing the EPG electrode and the Pt ring was vertically inserted into the water jacketed cell, which was then purged with Ar for 50−60 min. The anaerobic HER experiments were carried out in thoroughly degassed solutions (freeze−pump−thaw) to eliminate any competing electrocatalytic O_2 reduction. Background scans were performed under the same conditions with bare EPG electrodes. Linear sweep voltammetry (LSV) was performed at 300 rpm (rotations per minute) to investigate the electrocatalytic H_2 generation. For aerobic HER, the electrolytic solutions were used without any freeze−pump−thaw manipulations.

Measurement of ROS. The ROS represent the ratio of the catalytic O_2 reduction current in the disc and the H_2O_2 oxidation current observed in the Pt ring. The H_2O_2 produced due to incomplete O_2 reduction is radially defused out to the Pt ring where it is oxidized back to O_2 producing a oxidation current (i.e., current having an opposite sign of the O_2 reduction current). The collection efficiency (∼20−22%) is estimated before every new set of experiments using the ferrocyanide/ferricyanide redox system.

Controlled Potential Coulometry and Faradaic Yield. The controlled potential bulk electrolysis experiments were performed in the same water jacketed electrochemical cell that is used for the LSV. These experiments were performed in unbuffered degassed as well as aerated KPF_6 solutions with pH 5.5 at −0.7 V vs NHE for a particular time. The shaft bearing the working electrode was rotated at 600 rpm to disperse H_2 bubbles formed on electrolysis. During electrolysis the H_2 generated was collected through an outlet of the cell and collected using an inverted buret setup. The ratio of the moles of H_2 produced in the process (estimated from the volume of H_2 collected) and the charge dispersed is reported as the FY.

Detection of H_2. H_2 is generally detected by head space gas analysis by a GC fitted with TCD. Artero et al. reported an electrochemical method for detecting H_2 using rotating ring disc electrochemistry (RRDE). In an RRDE experiment a Pt ring encircling the working EPG electrode is held at a constant potential of 0.5 V. At this potential Pt electrode oxidizes H_2, generated at the working electrode and radially diffused outward to the Pt electrode because of the hydrodynamic current produced by the rotating shaft back to H^+, generating an oxidation current. Thus, a reduction current is observed at the working electrode and an oxidation current is observed at the Pt electrode. The viability of this method is previously established by this group by purging pure H_2 gas in the vicinity of a working Pt-wire electrode held at constant potential of 0.5 V; details are described in a previous report.[38] The gas evolved during BE was detected by using a GC instrument brought from Agilent Technologies with model no. 7890B (G3440B), serial no. CN14333203, fitted with TCD. Approximately 200 μL gas was collected by a gastight syringe and was injected into the inlet of the GC.

X-ray Photoelectron Spectroscopy. The EPG electrode was freshly polished with silicon carbide paper to get rid of all the contaminations for each single use. The complexes were dissolved in DCM (1 mM) , and 200 μL of solution was drop-casted prior to heterogeneous electrochemical investigations. Subsequently, Additional complex was removed by repeated washing with chloroform, ethanol, and water. Then long time anaerobic BE was done in unbuffered KPF_6 solution. After long-time BE, the EPG surface was washed with deionized water and ethanol and dried under Ar atmosphere. XPS (XPS, Omicron, model: 1712−62−11) measurement was done using a high resolution monochromatic Mg−Kα

DOI: 10.1021/jacs.8b05983
J. Am. Chem. Soc. 2018, 140, 12457−12468

radiation source at 1253.6 eV under 15 kV voltage and 5 mA current condition.

X-ray Structure Determinations. X-ray data were collected either at 150 K on a Bruker SMART APEX-II diffractometer with graphite-monochromated Mo Kα radiation (λ = 0.710 73 Å) controlled by the APEX 2 (v. 2010.1−2) software package (complexes **1** and **2**) or at 100 K on a Bruker D8VENTURE Microfocus diffractometer equipped with PHOTON II Detector, with Mo Kα radiation (λ = 0.710 73 Å), controlled by the APEX3 (v2017.3−0) software package (complex **3**). Raw data were integrated and corrected for Lorentz and polarization effects using the Bruker APEX II95/APEX III program suite. Absorption corrections were performed using SADABS. All the structures were solved by direct methods and were refined against all data in the reported 2θ ranges by full-matrix least-squares on F^2 with the SHELXL program suite98 using the OLEX 299 interface. Hydrogen atoms at idealized positions were included during the final refinements of each structure. The OLEX 2 interface was used for structure visualization, analysis of bond distances and angles, and drawing ORTEP100,101 plots.

■ ASSOCIATED CONTENT

Supporting Information

The Supporting Information is available free of charge on the ACS Publications website at DOI: 10.1021/jacs.8b05983.

Additional experimental details, spectroscopic data, and electrochemical data (PDF)

Crystal structures of complexes **1** (CIF), **2** (CIF), and **3** (CIF)

■ AUTHOR INFORMATION

Corresponding Authors

*icad@iacs.res.in

*marcetta@chem.tamu.edu

ORCID

Marcetta Y. Darensbourg: 0000-0002-0070-2075

Abhishek Dey: 0000-0002-9166-3349

Notes

The authors declare no competing financial interest.

■ ACKNOWLEDGMENTS

The research was funded by MNRE 103/180/2010-NT and CEFIPRA project 5405-1. E.A. acknowledges CSIR-SRF, and S.D. acknowledges IACS Institute Fellow Scheme. The XPS facility in IACS is funded by DST Nano Mission. M.Y.D. acknowledges the USA National Science Foundation for financial support (CHE-1266097 and CHE-1665258) and the Robert A. Welch Foundation (A-0924). Mr. N. Pal, Dr. R. Saha, Mr. M. Jana, and Mr. S. Khatua are greatly acknowledged for their assistance in structure determination.

■ REFERENCES

(1) Fontecilla-Camps, J. C.; Volbeda, A.; Cavazza, C.; Nicolet, Y. *Chem. Rev.* **2007**, *107*, 4273−4303.

(2) Vincent, K. A.; Parkin, A.; Armstrong, F. A. *Chem. Rev.* **2007**, *107*, 4366−4413.

(3) Lubitz, W.; Ogata, H.; Rüdiger, O.; Reijerse, E. *Chem. Rev.* **2014**, *114*, 4081−4148.

(4) Nicolet, Y.; Piras, C.; Legrand, P.; Hatchikian, C. E.; Fontecilla-Camps, J. C. *Structure* **1999**, *7*, 13−23.

(5) Peters, J. W.; Lanzilotta, W. N.; Lemon, B. J.; Seefeldt, L. C. *Science* **1998**, *282*, 1853.

(6) Rodríguez-Maciá, P.; Pawlak, K.; Rüdiger, O.; Reijerse, E. J.; Lubitz, W.; Birrell, J. A. *J. Am. Chem. Soc.* **2017**, *139*, 15122−15134.

(7) Adamska, A.; Silakov, A.; Lambertz, C.; Rüdiger, O.; Happe, T.; Reijerse, E.; Lubitz, W. *Angew. Chem., Int. Ed.* **2012**, *51*, 11458−11462.

(8) Silakov, A.; Wenk, B.; Reijerse, E.; Lubitz, W. *Phys. Chem. Chem. Phys.* **2009**, *11*, 6592−6599.

(9) Nicolet, Y.; de Lacey, A. L.; Vernède, X.; Fernandez, V. M.; Hatchikian, E. C.; Fontecilla-Camps, J. C. *J. Am. Chem. Soc.* **2001**, *123*, 1596−1601.

(10) Berggren, G.; Adamska, A.; Lambertz, C.; Simmons, T. R.; Esselborn, J.; Atta, M.; Gambarelli, S.; Mouesca, J. M.; Reijerse, E.; Lubitz, W.; Happe, T.; Artero, V.; Fontecave, M. *Nature* **2013**, *499*, 66−69.

(11) Barton, B. E.; Olsen, M. T.; Rauchfuss, T. B. *J. Am. Chem. Soc.* **2008**, *130*, 16834−16835.

(12) Carroll, M. E.; Barton, B. E.; Rauchfuss, T. B.; Carroll, P. J. *J. Am. Chem. Soc.* **2012**, *134*, 18843−18852.

(13) Sommer, C.; Adamska-Venkatesh, A.; Pawlak, K.; Birrell, J. A.; Rüdiger, O.; Reijerse, E. J.; Lubitz, W. *J. Am. Chem. Soc.* **2017**, *139*, 1440−1443.

(14) Adamska-Venkatesh, A.; Krawietz, D.; Siebel, J.; Weber, K.; Happe, T.; Reijerse, E.; Lubitz, W. *J. Am. Chem. Soc.* **2014**, *136*, 11339−11346.

(15) Orain, C.; Saujet, L.; Gauquelin, C.; Soucaille, P.; Meynial-Salles, I.; Baffert, C.; Fourmond, V.; Bottin, H.; Léger, C. *J. Am. Chem. Soc.* **2015**, *137*, 12580−12587.

(16) Baffert, C.; Demuez, M.; Cournac, L.; Burlat, B.; Guigliarelli, B.; Bertrand, P.; Girbal, L.; Léger, C. *Angew. Chem.* **2008**, *120*, 2082−2084.

(17) Kubas, A.; De Sancho, D.; Best, R. B.; Blumberger, J. *Angew. Chem., Int. Ed.* **2014**, *53*, 4081−4084.

(18) Stripp, S. T.; Goldet, G.; Brandmayr, C.; Sanganas, O.; Vincent, K. A.; Haumann, M.; Armstrong, F. A.; Happe, T. *Proc. Natl. Acad. Sci. U. S. A.* **2009**, *106*, 17331−17336.

(19) Lambertz, C.; Leidel, N.; Havelius, K. G. V.; Noth, J.; Chernev, P.; Winkler, M.; Happe, T.; Haumann, M. *J. Biol. Chem.* **2011**, *286*, 40614−40623.

(20) Bruska, M. K.; Stiebritz, M. T.; Reiher, M. *J. Am. Chem. Soc.* **2011**, *133*, 20588−20603.

(21) Stiebritz, M. T.; Reiher, M. *Inorg. Chem.* **2009**, *48*, 7127−7140.

(22) Hong, G.; Pachter, R. *ACS Chem. Biol.* **2012**, *7*, 1268−1275.

(23) Dey, S.; Rana, A.; Crouthers, D.; Mondal, B.; Das, P. K.; Darensbourg, M. Y.; Dey, A. *J. Am. Chem. Soc.* **2014**, *136*, 8847−8850.

(24) Kaeffer, N.; Morozan, A.; Artero, V. *J. Phys. Chem. B* **2015**, *119*, 13707−13713.

(25) Swanson, K. D.; Ratzloff, M. W.; Mulder, D. W.; Artz, J. H.; Ghose, S.; Hoffman, A.; White, S.; Zadvornyy, O. A.; Broderick, J. B.; Bothner, B.; King, P. W.; Peters, J. W. *J. Am. Chem. Soc.* **2015**, *137*, 1809−1816.

(26) Kubas, A.; Orain, C.; De Sancho, D.; Saujet, L.; Sensi, M.; Gauquelin, C.; Meynial-Salles, I.; Soucaille, P.; Bottin, H.; Baffert, C.; Fourmond, V.; Best, R. B.; Blumberger, J.; Léger, C. *Nat. Chem.* **2016**, *9*, 88.

(27) Horch, M.; Lauterbach, L.; Mroginski, M. A.; Hildebrandt, P.; Lenz, O.; Zebger, I. *J. Am. Chem. Soc.* **2015**, *137*, 2555−2564.

(28) Finkelmann, A. R.; Stiebritz, M. T.; Reiher, M. *Inorg. Chem.* **2014**, *53*, 11890−11902.

(29) Rodriguez-Macia, P.; Birrell, J. A.; Lubitz, W.; Rudiger, O. *ChemPlusChem* **2017**, *82*, 540−545.

(30) Lauterbach, L.; Lenz, O. *J. Am. Chem. Soc.* **2013**, *135*, 17897−17905.

(31) Wulff, P.; Day, C. C.; Sargent, F.; Armstrong, F. A. *Proc. Natl. Acad. Sci. U. S. A.* **2014**, *111*, 6606−6611.

(32) Esselborn, J.; Lambertz, C.; Adamska-Venkatesh, A.; Simmons, T.; Berggren, G.; Noth, J.; Siebel, J.; Hemschemeier, A.; Artero, V.; Reijerse, E.; Fontecave, M.; Lubitz, W.; Happe, T. *Nat. Chem. Biol.* **2013**, *9*, 607.

(33) Siebel, J. F.; Adamska-Venkatesh, A.; Weber, K.; Rumpel, S.; Reijerse, E.; Lubitz, W. *Biochemistry* **2015**, *54*, 1474−1483.

(34) Wilson, A. D.; Newell, R. H.; McNevin, M. J.; Muckerman, J. T.; Rakowski DuBois, M.; DuBois, D. L. *J. Am. Chem. Soc.* **2006**, *128*, 358−366.
(35) Franz, J. A.; O'Hagan, M.; Ho, M.-H.; Liu, T.; Helm, M. L.; Lense, S.; DuBois, D. L.; Shaw, W. J.; Appel, A. M.; Raugei, S.; Bullock, R. M. *Organometallics* **2013**, *32*, 7034−7042.
(36) Tard, C.; Pickett, C. J. *Chem. Rev.* **2009**, *109*, 2245−2274.
(37) Gloaguen, F.; Rauchfuss, T. B. *Chem. Soc. Rev.* **2009**, *38*, 100−108.
(38) Dey, S.; Rana, A.; Dey, S. G.; Dey, A. *ACS Catal.* **2013**, *3*, 429−436.
(39) Ahmed, M. E.; Dey, S.; Mondal, B.; Dey, A. *Chem. Commun.* **2017**, *53*, 8188.
(40) Quentel, F.; Passard, G.; Gloaguen, F. *Energy Environ. Sci.* **2012**, *5*, 7757−7761.
(41) Le Goff, A.; Artero, V.; Jousselme, B.; Tran, P. D.; Guillet, N.; Métayé, R.; Fihri, A.; Palacin, S.; Fontecave, M. *Science* **2009**, *326*, 1384.
(42) Gentil, S.; Lalaoui, N.; Dutta, A.; Nedellec, Y.; Cosnier, S.; Shaw, W. J.; Artero, V.; Le Goff, A. *Angew. Chem., Int. Ed.* **2017**, *56*, 1845−1849.
(43) Helm, M. L.; Stewart, M. P.; Bullock, R. M.; DuBois, M. R.; DuBois, D. L. *Science* **2011**, *333*, 863−866.
(44) Kilgore, U. J.; Roberts, J. A. S.; Pool, D. H.; Appel, A. M.; Stewart, M. P.; DuBois, M. R.; Dougherty, W. G.; Kassel, W. S.; Bullock, R. M.; DuBois, D. L. *J. Am. Chem. Soc.* **2011**, *133*, 5861−5872.
(45) Ott, S.; Borgström, M.; Kritikos, M.; Lomoth, R.; Bergquist, J.; Åkermark, B.; Hammarström, L.; Sun, L. *Inorg. Chem.* **2004**, *43*, 4683−4692.
(46) Lawrence, J. D.; Li, H.; Rauchfuss, T. B. *Chem. Commun.* **2001**, 1482−1483.
(47) Lawrence, J. D.; Li, H.; Rauchfuss, T. B.; Bénard, M.; Rohmer, M.-M. *Angew. Chem., Int. Ed.* **2001**, *40*, 1768−1771.
(48) Liu, T.; Wang, M.; Shi, Z.; Cui, H.; Dong, W.; Chen, J.; Åkermark, B.; Sun, L. *Chem. - Eur. J.* **2004**, *10*, 4474−4479.
(49) Jiang, S.; Liu, J.; Shi, Y.; Wang, Z.; Akermark, B.; Sun, L. *Dalton Trans.* **2007**, 896−902.
(50) Chong, D.; Georgakaki, I. P.; Mejia-Rodriguez, R.; Sanabria-Chinchilla, J.; Soriaga, M. P.; Darensbourg, M. Y. *Dalton Trans.* **2003**, 4158−4163.
(51) Ott, S.; Kritikos, M.; Åkermark, B.; Sun, L.; Lomoth, R. *Angew. Chem., Int. Ed.* **2004**, *43*, 1006−1009.
(52) Le Goff, A.; Artero, V.; Metayé, R.; Moggia, F.; Jousselme, B.; Razavet, M.; Tran, P. D.; Palacin, S.; Fontecave, M. *Int. J. Hydrogen Energy* **2010**, *35*, 10790−10796.
(53) Grim, S. O.; Matienzo, L. J.; Swartz, W. E. *J. Am. Chem. Soc.* **1972**, *94*, 5116−5117.
(54) Bard, A. J.; Faulkner, L. R. *Electrochemical Methods: Fundamentals and Applications*; WILEY-VCH Verlag GmbH: Weinheim, Germany, 2000.
(55) Vannucci, A. K.; Hull, J. F.; Chen, Z.; Binstead, R. A.; Concepcion, J. J.; Meyer, T. J. *J. Am. Chem. Soc.* **2012**, *134*, 3972−3975.
(56) Concepcion, J. J.; Binstead, R. A.; Alibabaei, L.; Meyer, T. J. *Inorg. Chem.* **2013**, *52*, 10744−10746.
(57) Chatterjee, S.; Sengupta, K.; Mondal, B.; Dey, S.; Dey, A. *Acc. Chem. Res.* **2017**, *50*, 1744−1753.
(58) Dey, S.; Mondal, B.; Chatterjee, S.; Rana, A.; Amanullah, S.; Dey, A. *Nat. Rev. Chem.* **2017**, *1*, 0098.
(59) Crouthers, D. J.; Denny, J. A.; Bethel, R. D.; Munoz, D. G.; Darensbourg, M. Y. *Organometallics* **2014**, *33*, 4747−4755.

DOI: 10.1021/jacs.8b05983
J. Am. Chem. Soc. 2018, 140, 12457−12468